Mon. Not. R. Astron. Soc. **000**, 1–14 (2014) Printed 1 December 2014 (MN LATEX style file v2.2)

One-dimensional non-LTE time-dependent radiative transfer of an He-detonation model and the connection to faint and fast-decaying supernovae

Luc Dessart[1] and D. John Hillier[2]

[1]: *Laboratoire Lagrange, UMR 7293, Université Nice Sophia-Antipolis, CNRS, Observatoire de la Côte dAzur, 06300 Nice, France.*
[2]: *Department of Physics and Astronomy & Pittsburgh Particle physics, Astrophysics, and Cosmology Center (PITT PACC), University of Pittsburgh, 3941 OHara Street, Pittsburgh, PA 15260, USA*

arXiv:1411.7397v1 [astro-ph.SR] 26 Nov 2014

Accepted 2014 November 25. Received 2014 November 24; in original form 2014 October 13

ABSTRACT

We present non-LTE time-dependent radiative transfer simulations for ejecta produced by the detonation of an helium shell at the surface of a low-mass carbon/oxygen white dwarf (WD). This mechanism is one possible origin for supernovae (SNe) with faint and fast-decaying light curves, such as .Ia SNe and Ca-rich transients. Our initial ejecta conditions at 1 d are given by the 0.18 B explosion model COp45HEp2 of Waldman et al.. The $0.2\,M_\odot$ ejecta initially contains $0.11\,M_\odot$ of He, $0.03\,M_\odot$ of Ca, and $0.03\,M_\odot$ of Ti. We obtain a $\sim$5 d rise to a bolometric maximum of $3.59\times10^{41}\,erg\,s^{-1}$, primarily powered by ^{48}V decay. Multi-band light curves show distinct morphologies, with a rise to maximum magnitude (-14.3 to -16.7 mag) that varies between 3 to 9 d from the U to the K bands. Near-IR light curves show no secondary maximum. Because of the presence of both He I and Si II lines at early times we obtain a hybrid Type Ia/Ib classification. During the photospheric phase line blanketing is caused primarily by Ti II. At nebular times, the spectra show strong Ca II lines in the optical (but no [O I] 6300–6364 Å emission), and Ti II in the near-IR. Overall, these results match qualitatively the very disparate properties of .Ia SNe and Ca-rich transients. Although the strong Ti II blanketing and red colors that we predict are rarely observed, they are seen, for example, in OGLE-2013- SN-079. Furthermore, we obtain a faster light-curve evolution than, for example, PTF10iuv, indicating an ejecta mass $> 0.2\,M_\odot$. An alternate scenario may be the merger of two WDs, one or both composed of He.

Key words: radiative transfer – supernovae: general – supernovae: individual: SN 2005E, PTF09dav, PTF10iuv, OGLE-2013-SN-079.

1 INTRODUCTION

Helium-shell detonations at the surface of CO white dwarfs (WDs) have been studied a number of times over the last 30 years (see, e.g., Taam 1980; Woosley & Weaver 1994; Livne & Glasner 1990, 1991; Livne & Arnett 1995; Bildsten et al. 2007). The ignition conditions are complex, making the subsequent evolution of the burning shell uncertain. Further, the properties of the accreted helium shell at detonation depends on the CO WD mass. These variations in properties are known to considerably alter the nucleosynthetic yields, with the production of intermediate-mass elements (IMEs) favored at lower density (see, e.g., Shen et al. 2010; Waldman et al. 2011) and iron-group elements (IGEs) favored at higher densities (Fink et al. 2007). Furthermore, for higher mass CO WDs, the surface detonation may cause the detonation of the core, leading to a full disruption of the system rather than a shell ejection. Lacking a well defined model for the detonations of such shells (e.g., initial density/radial structure for the shell, mechanism of ignition, evolution of the combustion, multi-dimensional effects, etc.), it is unclear what scenarios occur, and with what frequencies. Although He-shell detonations are unlikely to produce the population of standard SNe Ia (Fink et al. 2007), they represent physical conditions that may occur in Nature and thus warrant study.

Renewed interest in helium-shell detonations has come from the recent discovery of rare transients characterized by

(i) a fast-evolving light curve with a modest peak brightness (by SN standards);
(ii) a peculiar composition revealed through the presence of spectral signatures from helium and IMEs (e.g., Ti, Ca, Sc) and inferred (for SN 2005E) from nebular line analyses (Perets et al. 2010; Sullivan et al. 2011; Kasliwal et al. 2012);
(iii) the Ca II-dominated optical spectra at nebular times, with no signature from IGEs.

They exhibit standard line widths during the high-brightness phase,

© 2014 RAS

suggesting the expansion rate is comparable to standard-energy SNe. The faster evolving light curves suggest, however, a lower ejecta mass. These extraordinary SNe Ib are associated with old stellar populations (Perets et al. 2011) located at large distances from their hosts (Kasliwal et al. 2012), rather than with star forming regions rich in massive stars (Anderson & James 2009). Prototypical events of that class are SN 2005E, SN 2007ke, PTF 09dav, PTF 10iuv, and PTF 11bij.

Another class of fast-evolving transients are Type Iax SNe — the prototypical member of the SN Iax class is SN 2002cx. Relative to standard SNe Ia, these SNe have narrower spectral lines and are fainter by $\gtrsim 1$ mag at maximum; they also have blue early-time spectra reminiscent of SN 1991T (Foley et al. 2013). The origin of SNe Iax is debated. They may stem from low-energy deflagrations (Jordan et al. 2012; Fink et al. 2014), or perhaps double detonations in sub-Chandrasekhar white dwarfs (see, e.g., Sim et al. 2012). Their spectra differ from SN 2005E, with the most extreme narrow lined member, SN 2008ha, having a spectrum dominated by IMEs. Foley et al. (2013) excluded SN 2005E from the Iax class on the basis of its somewhat distinct spectra from the prototype SN 2002cx and its association with an early-type galaxy since Type Iax SNe tend to be associated with late-type galaxies. Foley et al. (2013) raise the possibility that SN 2005E arose through accretion from a degenerate He star, rather than from a non-degenerate He star proposed for the Iax class.

Radiative-transfer simulations of helium-shell detonations have been performed by Perets et al. (2010), who focused on nebular-phase spectra to emphasize the large abundance of Ca over IGEs and the unique nature of these events. Waldman et al. (2011) performed a set of simulations for 0.15-0.3 $M_\odot$ He shells detonating on low-mass CO WDs of 0.4-0.6 $M_\odot$. Their radiative-transfer modeling is centered on their model COp45HEp2 and a confrontation to SN 2005E. Shen et al. (2010) performed a set of simulations for similar He shells but typically associated with higher mass CO WDs, leading to large differences in yields, light curves, and spectra. Despite the diversity of ejecta and radiation properties (and the mismatches to observations), these simulations suggest that He-shell detonations provide a promising framework for understanding .Ia SNe, Ca-rich transients, and more generally faint and fast transients associated with white-dwarf explosions.

In this paper we revisit these simulations. We focus on model COp45HEp2 of Waldman et al. (2011) but this time perform non-Local-Thermodynamic-Equilibrium (non-LTE) time-dependent simulations of the full ejecta. This multi-epoch study extends from 1.1 until ~ 60 d after the explosion. The non-LTE approach takes explicit account of non-thermal processes and allows for γ-ray escape and non-local energy deposition. This is critical since helium represents about one half of the ejecta mass and this new class of fast transients shows He I lines (hence the SN Ib classification) — all simulations so far have ignored non-thermal processes and produced synthetic spectra with no He I lines. Model bolometric and multi-band photometric light curves, and spectra, are compared to the well observed SN PTF 10iuv (Kasliwal et al. 2012). To address the spectral diversity of this class, we also compare the model to SNe 2005E (Perets et al. 2010) and PTF 09dav (Sullivan et al. 2011).

In Section 2, we present the observational data we use in this paper. The numerical setup and the initial ejecta conditions for our radiative transfer simulations with CMFGEN are discussed in Section 3. For details on our approach, we refer the reader to Dessart & Hillier (2005, 2008, 2010, 2011); Dessart et al. (2012); Li et al. (2012); Hillier & Dessart (2012); Dessart et al. (2014b).

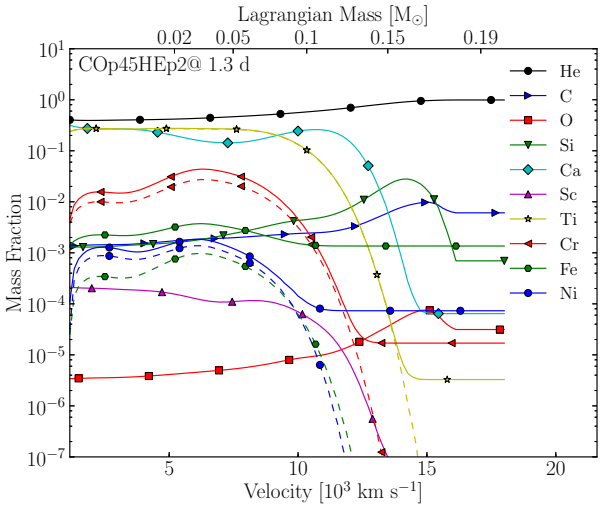

Figure 1. Composition of the ejecta model COp45HEp2 at a time of 1.16 d after explosion as a function of velocity (bottom axis) and Lagrangian mass coordinate (top axis). We also show the contributions of the dominant unstable isotope (dashed lines) for species Ti, Cr, Fe, and Ni. These isotopes are ^{44}Ti (yellow/star), ^{48}Cr (red/triangle), ^{52}Fe (green/hexagon), and ^{56}Ni (blue/circle).

We then present the results from our simulations, first describing the evolution of the ejecta properties (Section 5), and then those of the radiation, for both photometry (Section 6) and spectroscopy (Section 7). We digress on the estimate of the calcium mass and the oxygen mass from nebular spectra in Sections 8 and 9. In Section 10, we confront our model results to observations and present our conclusions.

2 OBSERVATIONS

To confront our model predictions to observations, we select a few fast evolving transients, including PTF10iuv (Kasliwal et al. 2012), SN 2005E (Perets et al. 2010), and PTF09dav (Sullivan et al. 2011). For PTF10uiv, we adopt a distance modulus of 35.1, a redshift of 0.0251485, and we assume no reddening (Kasliwal et al. 2012). For SN 2005E (PTF 09dav), we use a redshift of 0.00816565 (0.04) and neglect reddening (which is believed to be very small; Perets et al. 2010; Sullivan et al. 2011). We also adopt a distance of 34 Mpc for SN 2005E. The data shown in this paper was retrieved from the WISEREP website (Yaron & Gal-Yam 2012).

3 NUMERICAL SETUP AND INITIAL CONDITIONS

Waldman et al. (2011) studied the detonation of helium shells with a mass in the range 0.15-0.3 $M_\odot$ resting at the surface of CO WDs of 0.4-0.6 $M_\odot$. Based on the rough agreement of their model COp45HEp2 model with SN 2005E, considered as the prototype of Ca-rich transients (Perets et al. 2010), we utilize the same model. In the future, we will investigate other configurations to characterize common and distinct properties of the members of that class.

The ejecta model COp45HEp2 is characterized by a mass of 0.2 $M_\odot$ and a kinetic energy of 0.18 B. The total yields for the main species are given in Table 1. Helium represents half the total ejecta mass while carbon has a mass fraction of ~ 0.001 throughout the ejecta (a value close to solar). Oxygen is not a final yield of the

Table 1. Summary of ejecta properties for the helium detonation model COp45HEp2. We give the masses for the different species at a post-explosion time of 1.16 d, which is the start time of our CMFGEN simulations. However, for the isotopes that are unstable (last four columns; subscript o), we give their mass immediately after the combustion stops, i.e., prior to any decay. This is why the $^{48}Cr_o$ (given at 0 d) is larger than the Cr mass (given at 1.16 d).

E_{kin} [B]	M_{ejecta} [$M_\odot$]	He [$M_\odot$]	C [$M_\odot$]	O [$M_\odot$]	Si [$M_\odot$]	Ca [$M_\odot$]	Sc [$M_\odot$]	Ti [$M_\odot$]	Cr [$M_\odot$]	$^{44}Ti_o$ [$M_\odot$]	$^{48}Cr_o$ [$M_\odot$]	$^{52}Fe_o$ [$M_\odot$]	$^{56}Ni_o$ [$M_\odot$]
0.18	0.2	1.12(-1)	5.46(-4)	2.32(-6)	1.03(-3)	3.39(-2)	1.71(-5)	3.29(-2)	2.68(-3)	3.25(-2)	5.60(-3)	8.64(-4)	1.13(-4)

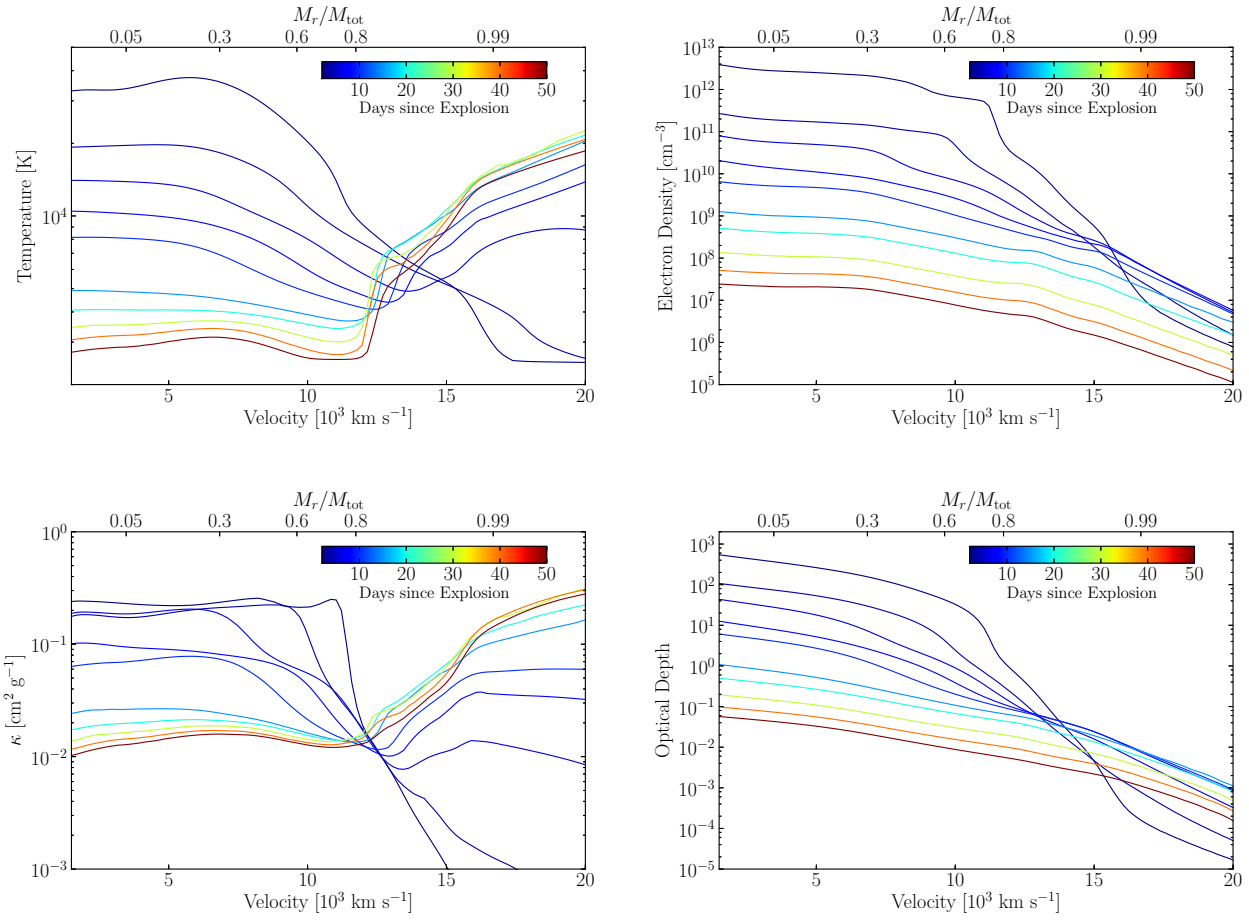

Figure 2. Evolution versus velocity (bottom axis) and fractional Lagrangian mass (top axis) of the ejecta temperature, the electron density, the Rosseland-mean opacity κ and the associated optical depth. The times shown are 2, 4, 6, 8, 10, 15, 20, 30, 40, 50 d after explosion. The total ejecta mass M_{tot} is 0.2 $M_\odot$.

combustion and ends up with an underproduction of ~ 100 compared to solar. For IMEs, the situation is disparate with elements such as Si and S having mass fractions on the order of only ~ 0.001 (thus significantly less than for the combustion of CO-rich material in SNe Ia progenitors but nonetheless somewhat larger than the solar values). On the other hand, for Ti, Ca, and Cr, the overproduction compared to solar metallicity, prior to any decay, is on the order of 10^3-10^4. This contrast is easily seen in Fig. 1 when comparing the composition between the deep layers of the ejecta (affected by combustion) and the outermost layers (where we adopt a solar mixture for metals).

We perform slight adjustments to the original ejecta produced by the hydrodynamical simulation (Waldman et al. 2011). We smooth the density and elemental distribution to reduce sharp gradients,[1] which are largely an artifact of the 1-D treatment of the explosion. To ensure the outer boundary is optically thin at early times, we also replace and extend the density structure beyond 16000 km s^{-1} by a power law in velocity with an exponent of -12 (the original density profile is poorly resolved and noisy at large velocities). The radiative-transfer simulations for model COp45HEp2 are started at 10^5 seconds after explosion and employ 100 grid points. The ejecta is in homologous expansion and covers velocities from 1100 to 29000 km s^{-1} (the outer radius is thus initially at 2.9×10^{14} cm). The outer ejecta temperature (mass density) is ~ 2000 K ($\sim 10^{-15}$ g cm^{-3}) so that the outer grid is transparent

[1] The smoothing is obtained by convolving the corresponding distributions with a gaussian whose standard deviation is 500 km s^{-1}.

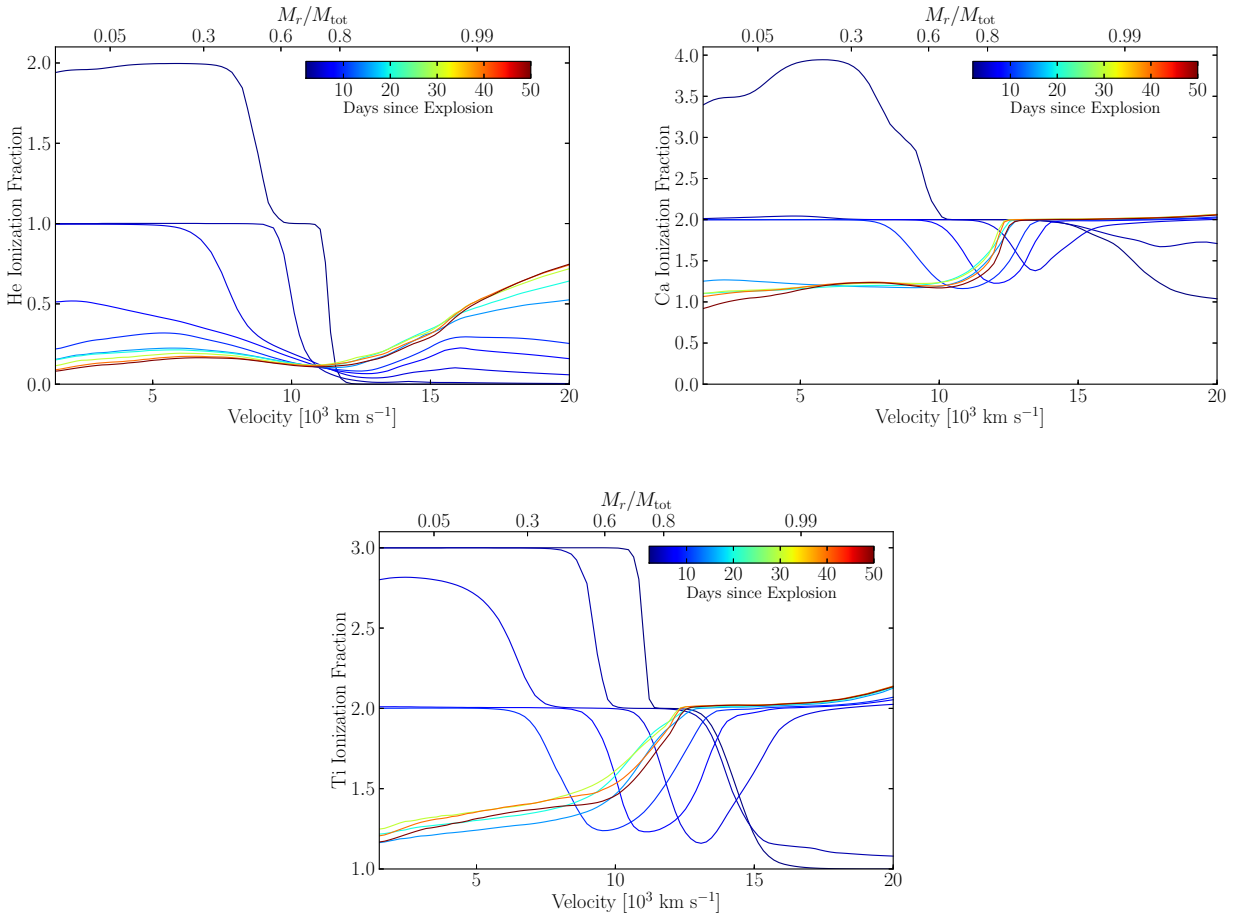

Figure 3. Same as Fig. 2, but now showing the helium, calcium, and titanium ionization states at the photosphere (a value of zero corresponds to a neutral state, of value of i to an ith-ionized atom). Note that the ordinate range varies amongst panels. The times plotted are 2, 4, 6, 8, 10, 15, 20, 30, 40, and 50 d after explosion.

to radiation. Further details on the COp45HEp2 model properties at 1.16 d can be found in Waldman et al. (2011).

In CMFGEN, the radiative transfer solver used is generally the same whatever the SN ejecta under study. What differs are the initial conditions (mass, density, explosion energy, composition etc.) and the model atoms employed. For this work, we use the model atom set named A3 in Dessart et al. (2014b), with several adjustments. We add He I and He II, as well as neutral states of Mg, Si, S, and Ca. We also employ a large Ti II model atom with 1000 levels (61 super levels). We treat nine two-step decay chains, whose leading isotope are ^{56}Ni, ^{57}Ni, ^{48}Cr, ^{49}Cr, ^{51}Mn, ^{55}Co, ^{37}K, ^{52}Fe, and ^{44}Ti. The characteristics of these chains are summarized in Dessart et al. (2014b). Non-local energy deposition is allowed for once the model reaches an age of 3 d — prior to that time we assume all the radioactive energy is deposited at the site of decay. However, at all times, we assume that positrons are destroyed locally, and hence their kinetic energy is deposited locally, i.e., at the site of emission. This is done for convenience since we lack late-time observations to constrain adequately the positron trapping efficiency. This efficiency should be high over the 1-2 months time scale considered here, although positrons injected through ^{44}Sc decay may increasingly escape, in the absence of a magnetic field, as the ejecta ages (Milne et al. 1999; Perets 2014).

There are several deficiencies in our models related to the atomic data. In particular, we do not have accurate photoionization cross-sections for Ti, and this could potentially impact the influence of Ti II on the spectra through an incorrect ionization balance. Further, in most of our modeling we did not allow for the influence of Vanadium on the spectrum – we simply included one level of V I in order to track the changes in composition associated with the ^{48}Cr $\rightarrow$ ^{48}V $\rightarrow$ ^{48}Ti decay chain. Limited testing with newly developed Ti and V atoms show only limited changes of the predicted spectra.

4 POWER SOURCE FOR RADIATION

Immediately after explosion, the most abundant unstable isotopes in model COp45HEp2 are ^{44}Ti, ^{48}Cr, ^{52}Fe, and ^{56}Ni (shown as dashed lines in Fig. 1), with initial masses of 0.033, 0.0056, 0.0009, and 0.0001 M$_\odot$, respectively. The isotope ^{44}Ti, which decays to ^{44}Ca via ^{44}Sc, is the primary constituent of Ti initially. Despite the large abundance, its very large half life of 21915 days makes it a secondary power source during the first 1-2 months after explosion. Conversely, the very short half lives (0.34479 and 0.01472 days) of ^{52}Fe and its daughter isotope ^{52}Mn make them weak power sources beyond a day. In our ejecta model, the main power source is the chain ^{48}Cr $\rightarrow$ ^{48}V $\rightarrow$ ^{48}Ti. ^{48}Cr has a half-life of

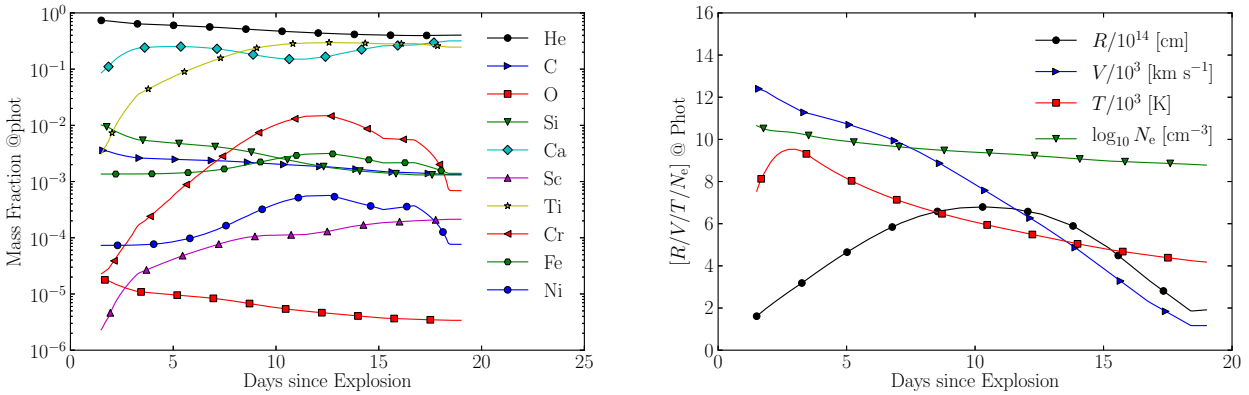

Figure 4. *Left:* Evolution at the photosphere of the mass fraction for He, C, O, Si, Ca, Sc, Ti, Cr, Fe, and Ni. We define the photosphere as the ejecta location where the inward-integrated Rosseland-mean optical depth is 2/3. The photosphere, defined that way, reaches the base of the ejecta at 18.4 d after explosion. *Right:* Same as left, but now showing the evolution of the radius, velocity, temperature, and electron density (with appropriate scalings) at the photosphere as a function of time. If we use electron scattering instead of the Rosseland-mean opacity for the definition of the photosphere, these curves are shifted by ~ 10 %.

0.89833 d and releases 0.430 MeV per decay while ^{48}V has a half-life of 15.9735 d and releases 3.0553 MeV (of which 0.1449 MeV is positron energy) per decay. The energy per decay is comparable to the ^{56}Ni chain (total of 5.4671 MeV), but with a shorter characteristic time. However, the low mass of ^{48}Cr in this ejecta can only generate a small power compared to SNe Ia, which have approximately 100 times more ^{56}Ni.

5 RESULTS: EJECTA PROPERTIES

Of particular interest are the temperature, the ionization state, and the electron density because they control the ejecta optical depth and the ions present at the photosphere. Figures 2 and 3 illustrate these quantities.

The ejecta optical depth, temperature and ionization are interrelated. For as long as the temperature stays above ~ 10000 K (Fig. 2), helium, which is the dominant species at all ejecta locations, remains partially (or fully) ionized (Fig. 3). Early on, the separation between ionized and partially neutral regions is the photosphere — it coincides with the jump in electron density and in helium ionization (Fig. 3). When the ejecta temperature drops everywhere below ~ 10000 K, helium recombines to its neutral state, the mass absorption coefficient (here, we use the Rosseland-mean opacity, which becomes merely indicative when the conditions turn optically thin) suddenly decreases, and the ejecta optical depth drops below unity. The opacity is also function of the density and the temperature (which affects collisional processes, level populations etc.) but the electron density (and the process of electron scattering) is key for the gas opacity. At 2 d after explosion, the outer 30 % of the ejecta is neutral and optically thin to radiation. Assuming a constant opacity with depth and time is therefore inaccurate. Although the temperature continuously decreases at velocities less than 11000 km s^{-1}, non-thermal processes maintain a persistent He^+ population with an ionization fraction of ~ 5% or larger.

When the conditions are ionized, we find that non-thermal processes play little or no role and the entire decay energy is deposited as heat (Xu et al. 1991; Dessart et al. 2012; Li et al. 2012). At and above the photosphere (and throughout the ejecta when it turns thin), the fraction of the decay energy channeled into non-thermal ionization and excitation at the photosphere is ~ 20 % and 10 %, respectively. As discussed in Section 7, this causes the production of He I lines at light curve peak.

The evolution of the photospheric properties is shown in Fig. 4. The photospheric mass fraction of He and of IGEs evolves little with time, but increases by 1-2 orders of magnitude for IMEs, especially for Sc, Ti, and Cr. This evolution is primarily caused by the chemical stratification rather than radioactive decay. The photosphere reaches a maximum radius of 6×10^{14} cm at 10 d. Prior to that, the photosphere moves at a velocity in excess of 7000 km s^{-1}; this is in the range of photospheric velocities seen in Ca-rich transients at early times (Perets et al. 2010; Kasliwal et al. 2012). Photospheric temperatures are in the range 4000–8000 K and will cause the presence of lines from neutral and once-ionized species in spectra. The most abundant species at the photosphere (in fact, at all depths and thus at all times) are He, Ca, and Ti.

6 RESULTS: BOLOMETRIC LUMINOSITY AND MULTI-BAND LIGHT CURVES

The bolometric light curve of model COp45HEp2 shows a very rapid evolution, with a peak of 3.59×10^{41} erg s^{-1} at only 5.17 d after explosion (left panel of Fig. 5). For comparison, standard-energy delayed-detonation models of Chandrasekhar-mass WDs give a bolometric maximum of $\sim10^{43}$ erg s^{-1} and a rise time of $\sim$18 d (Blondin et al. 2013). These differences stem from the greater decay energy released in SNe Ia (the mass of ^{56}Ni is 100 times greater in standard SNe Ia than the mass of ^{48}Cr in model COp45HEp2) and the larger ejecta mass in SNe Ia (1.4 compared to 0.2 $M_\odot$ in model COp45HEp2). The energy to mass ratio is however comparable between a typical SN Ia and the He-shell detonation model COp45HEp2.

At maximum, the luminosity is comparable to the decay power (Fig. 5), as expected (Arnett 1982) and obtained for SNe Ia (Hoeflich & Khokhlov 1996; Blondin et al. 2013). Past maximum, it exceeds the decay power until it turns optically thin at about two weeks after explosion. This excess stems from stored energy within

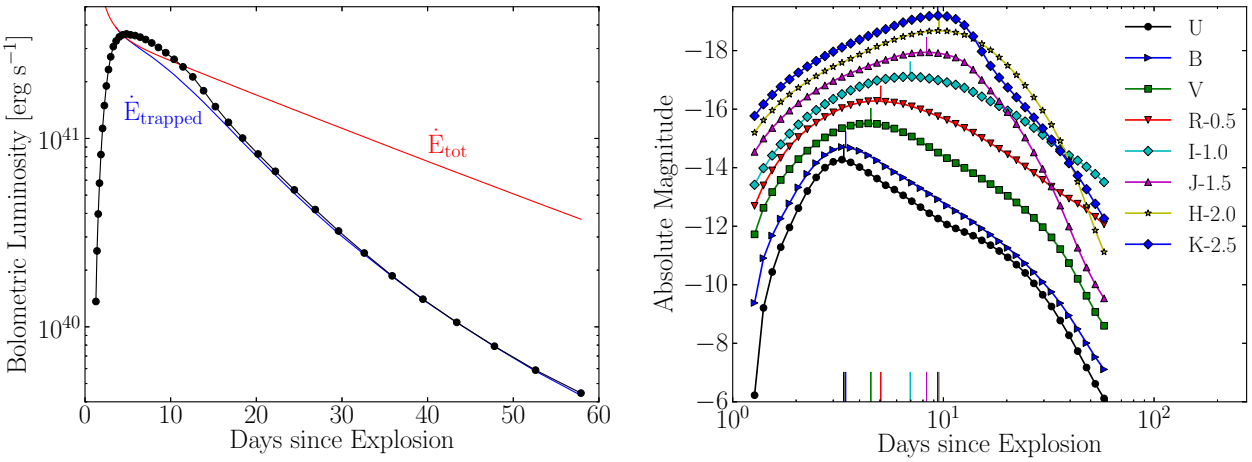

Figure 5. *Left:* Bolometric luminosity of model COp45HEp2. We also add the total decay energy power (red) and the fraction that is trapped within the ejecta (blue). The time of bolometric maximum is 4.84 d after explosion. *Right:* Same as left, but now for the multi-band light curves. Tick marks at bottom indicate the rise time in each filter. In contrast, standard SNe Ia have a bolometric maximum of $\sim 10^{43}$ erg s^{-1} at ~ 18 d after explosion, and exhibit a secondary maximum in near-IR bands.

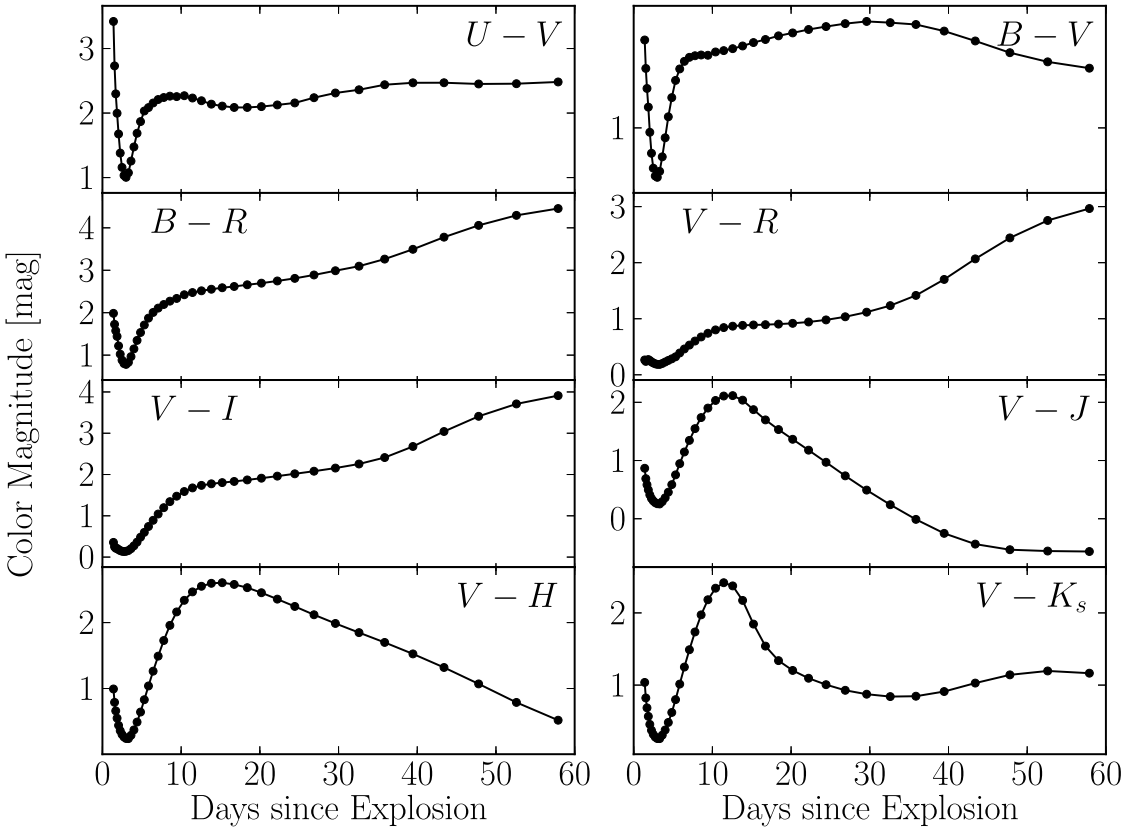

Figure 6. Illustration of the color evolution of model COp45HEp2 for different filter combinations.

the ejecta and remains visible as long as the energy can be trapped. The model luminosity around light curve maximum is powered at the $\gtrsim$95 % level by the decay of ^{48}Cr and its daughter element ^{48}V. The escape of γ rays starts around maximum (blue versus red curve) and causes a large leakage of energy — by 60 d after explosion only $\sim$ 10% of the total decay energy is trapped.

These properties are consistent with the heuristic estimates of Bildsten et al. (2007). We find a bolometric maximum 30 % higher and a rise time that is 30% shorter than obtained by Waldman et al. (2011) for that same model. The reason for this is probably that they adopt a gray opacity, approximate its dependency on composition, and ignore the influence of ionization. Still, the key feature of a very short rise time to a modest maximum bolometric luminosity remains. In general, adopting a fixed mass absorption coefficient or

applying simple scalings based on SN Ia ejecta (Perets et al. 2010) will probably lead to an overestimate of the opacity and an underestimate of the ejecta mass (see Section 10).

Multi-band light curves show large variations between filters (right panel of Fig. 5). Rise times to maximum increase monotonically with the mean wavelength of each filter. The times of maximum magnitude are 3.37 (U), 3.44 (B), 4.53 (V), 5.04 (R), 7.07 (I), 8.38 (J), 9.62 (H), and 9.37 d (K). The fading rate past maximum varies with time and differs significantly between filters. For example, the magnitude fading between maximum and 15 days later covers the large range from 1.3 to $\gtrsim 3$ mag (Table 2). Interestingly, the near-IR bands show no secondary maximum, in contrast to standard SN Ia explosions. There are probably several reasons for this, including the difference in temperature evolution (our model is cool and has red colors even at peak), in ionization (Ca and Ti remain once ionized after bolometric maximum), and in composition (the Co intimately related to the secondary maximum of SNe Ia is strongly under-abundant in our COp45HEp2 model). We do not dwell further upon this issue since there is at present no near-IR observation (neither photometric nor spectroscopic) of .Ia SNe and Ca-rich transients.

During the photospheric phase (i.e. prior to ~ 20 d), the color evolution of model COp45HEp2 in the optical and near-IR is towards bluer colors up to the peak and then redder (Fig. 6). When the ejecta turns thin (which occurs around 18 d after explosion, depending on what opacity is used for the inference), the color evolution differs between filters. For example, $V-H$ decreases again (color shift to blue), while $U-V$ is roughly constant and $B-R$ increases (color shift to red). This complex behavior is related to the presence of strong emission lines (primarily forbidden) whose wavelength distribution coincidently overlap, or not, with specific filters. We discuss these spectral characteristics in the next section.

7 RESULTS: SPECTRA

A striking property of model COp45HEp2 is the unambiguous presence of He I lines in the optical and near-IR ranges around maximum brightness (i.e., from 5 to 15 d after explosion; Fig. 7). At maximum brightness, the He mass fraction at the photosphere is 0.6 (Fig. 4). As in standard SNe Ib, He I lines arise from efficient non-thermal excitation and ionization (Lucy 1991). In the optical, we see He I lines at 5875.66 ($3d\,^3D - 2p\,^3P^o$), 6678.15 ($3d\,^1D - 2p\,^1P^o$), and 7065.25 Å ($3s\,^3S - 2p\,^3P^o$). Si II 6347–6371 Å ($4p\,^2P^o - 4s\,^2S$ doublet) causes a strong feature up until bolometric maximum (i.e., ~ 4 d) and therefore produces a unique classification to this event as both a SN Ib and a SN Ia. There is also a broad absorption around 5000-5600 Å caused by S II (numerous transitions associated with the term 4p–4s). The same features affect the spectra of SNe Ia (there, the Si and S abundances are higher but the lines are typically saturated). No line of O I is seen anywhere in the model spectrum — the O mass fraction is only $\sim 2\times10^{-6}$. A test calculation with the oxygen abundance increased by a factor of 100 had no effect.

Calcium shows the usual strong optical lines with Ca II H&K ($4s\,^2S - 4p\,^2P^o$ terms), the triplet lines around 8500 Å ($3d\,^2D - 4p\,^2P^o$ terms), and the forbidden transitions at 7307 Å ($4s\,^2S - 3d\,^2D$ terms). These forbidden lines appear as early as 20 d after explosion in our simulations, just as the Rosseland-mean optical depth drops below unity. Scandium contributes some moderate blanketing (below ~ 10000km s^{-1}, its mass fraction is up by four orders of magnitude above the solar metallicity value). Two strong and broad features are unambiguously seen, at 5600 Å (terms $3p^6\,3d\,4p\,^3P^o - 3p^6\,3d^2\,^3P$) and at 6260 Å (terms $3p^6\,3d\,4p\,^3D^o - 3p^6\,3d^2\,^3P$).

With an ejecta mass fraction everywhere above ~ 0.1, titanium has the strongest impact on the spectrum. In the optical it causes significant blanketing in the blue and emission in the red, and is seen over the first month. It affects other strong spectral features, causing significant absorption that overlaps with He I 5875 Å and the forbidden doublet of Ca II. It can also lead to confusion with O I – the feature at ~ 7700 Å is due to Ti II rather than O I. The forest of Ti II lines in the optical corresponds to thousands of transitions that are not possible to list. For example, strong transitions occur between upper levels $3d^2(^3F)\,4p\,z\,^4D^o$ ($z\,^2P^o$ etc.) and lower levels like $3d^2(^3P)\,4s\,b\,^4P$. Although Ti is not considered an IGE, its complex atomic structure can cause dramatic line blanketing. Ti II line blanketing is so strong that it overwhelms the negligible blanketing associated with the much less abundant Fe II. Combined with the modest temperature of the photosphere, it causes the red color of the model at all times, even around bolometric maximum.

The near-IR range contains fewer spectral features (see right panel of Fig. 7). We obtain strong He I 10830 Å and a weaker He I 20581 Å. Ca II ($5s^2S - 5p^2P^o$) gives a strong feature at 11839 Å. All other lines are due to Ti II, in particular forbidden transitions associated with upper levels $3d^2(^3F)\,4p\,z\,^4F^o$ (and $z\,^2D^o$) and lower levels $3d\,4s^2\,c\,^2D$ ($3d^3\,b\,^2F$) with wavelengths 10113.87, 13320.45, 14151.54, 14631.55, 14711.64, 15231.10, and 15873.64 Å. Interestingly, it is the strengthening and weakening of these lines that control the near-IR photometry. In particular, the extended brightness in the H-band (which encompasses the range 1.5–1.8 μm) up to 20 d after explosion is caused by [Ti II]. In such ejecta, the near-IR range is the ideal place to search for signatures of Ti, determine its abundance, and quantify the extent to which it contributes to the ^{44}Ca enrichment of the ISM (Mulchaey et al. 2014).

By the end of our simulations, the only lines present in the optical and near-IR are He I 10830 Å and the forbidden line transitions of Ca II (7307 Å doublet) and Ti II (four strong transitions in the near-IR). The distinguishing feature of these events is not the presence of [Ca II], which is a common property of most SNe, either core collapse or thermonuclear. [Ca II] transitions are strong because they are the key coolants of SN ejecta, in particular when other species/lines are not present to compete (e.g., the $3d^6\,^5D - 3d^6\,^3F$ transition of Fe III at 4658.0 Å or the $3d^7\,^4F - 3d^7\,^2G$ transition of Co III at 5888.5 in SNe Ia; Hα in SNe II). The distinguishing feature of this model, and the class of so-called Ca-rich transients, is the lack of other strong lines at nebular times. Other distinct features are the presence of He I and Si II lines in the photospheric phase, causing a hybrid classification as Type Ib and Ia.

The morphology of individual lines is often affected by overlap and blanketing. Nonetheless, for strong lines, an identification is obvious and one can measure the velocity at maximum absorption to infer the typical expansion rate of the ejecta. We show a set of spectral montages focusing on He I 5875 Å, Si II 6355 Å, Ca II 7307 Å and He I 10830 Å in Fig. 8, restricting the time range to epochs when the features are the strongest. All these lines suggest a typical expansion rate of 10000 km s^{-1}, quite typical of Ca-rich transients studied here (Perets et al. 2010; Waldman et al. 2011; Kasliwal et al. 2012). Note that half the ejecta mass lies beyond 10000 km s^{-1} in our model (Fig. 1).

Previous simulations of helium-shell detonations neglected non-thermal processes and failed to produce He I lines (Shen et al. 2010; Waldman et al. 2011). Here, despite the rather uniform He mass fraction, we find these lines are not always present. In the op-

Table 2. Summary of photometric properties for model COp45HEp2. For each entry, we give the rise time to maximum, the value at maximum, and the magnitude change between peak and 15 d later for the corresponding filter band. Numbers in parentheses are powers of ten.

L_{bol}			L_{UBVRI}			U			B		
$t_{\rm rise}$ [d]	Max. erg s^{-1}	ΔM_{15} mag	$t_{\rm rise}$ [d]	Max. erg s^{-1}	ΔM_{15} mag	$t_{\rm rise}$ [d]	Max. mag	ΔM_{15} mag	$t_{\rm rise}$ [d]	Max. mag	ΔM_{15} mag
5.171(0)	3.590(41)	1.591(0)	4.330(0)	2.640(41)	1.714(0)	3.367(0)	-1.428(1)	3.124(0)	3.438(0)	-1.472(1)	3.236(0)
V			R			I					
$t_{\rm rise}$ [d]	Max. mag	ΔM_{15} mag	$t_{\rm rise}$ [d]	Max. mag	ΔM_{15} mag	$t_{\rm rise}$ [d]	Max. mag	ΔM_{15} mag			
4.526(0)	-1.552(1)	2.401(0)	5.044(0)	-1.578(1)	1.807(0)	7.065(0)	-1.610(1)	1.318(0)			
J			H			K					
$t_{\rm rise}$ [d]	Max. mag	ΔM_{15} mag	$t_{\rm rise}$ [d]	Max. mag	ΔM_{15} mag	$t_{\rm rise}$ [d]	Max. mag	ΔM_{15} mag			
8.378(0)	-1.644(1)	2.694(0)	9.622(0)	-1.668(1)	1.904(0)	9.369(0)	-1.669(1)	3.116(0)			

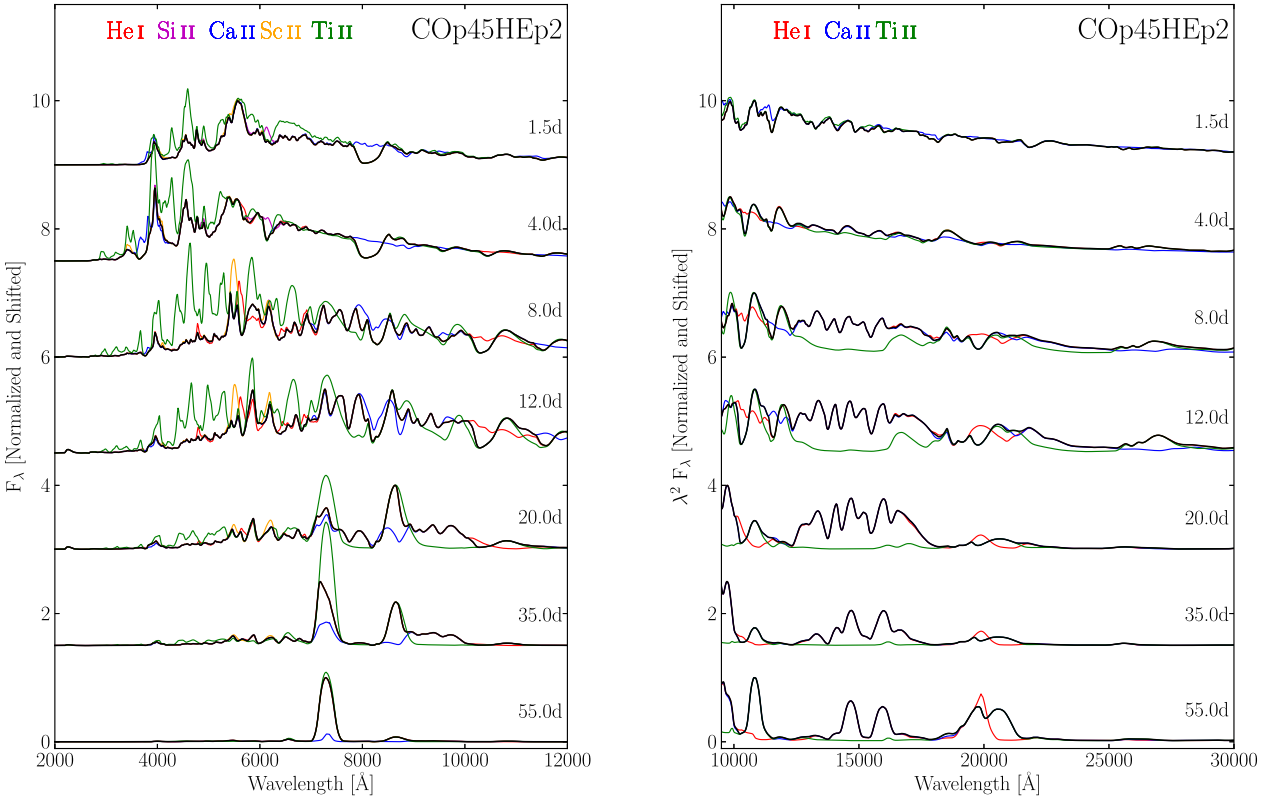

Figure 7. *Left:* Montage of synthetic spectra for model COp45HEp2 over the optical range, from 1.5 until 55 d. To facilitate the interpretation of the spectral features, we add synthetic spectra (color) where the bound-bound transitions of a selected ion (see label at top) is excluded from the spectrum calculation. A vertical shift of 1.5 is applied to each epoch (the flux at $\sim$2000 Å is close to zero at all times). *Right:* Same as leff, but now showing the quantity $\lambda^2 F_\lambda$ in the near-IR range.

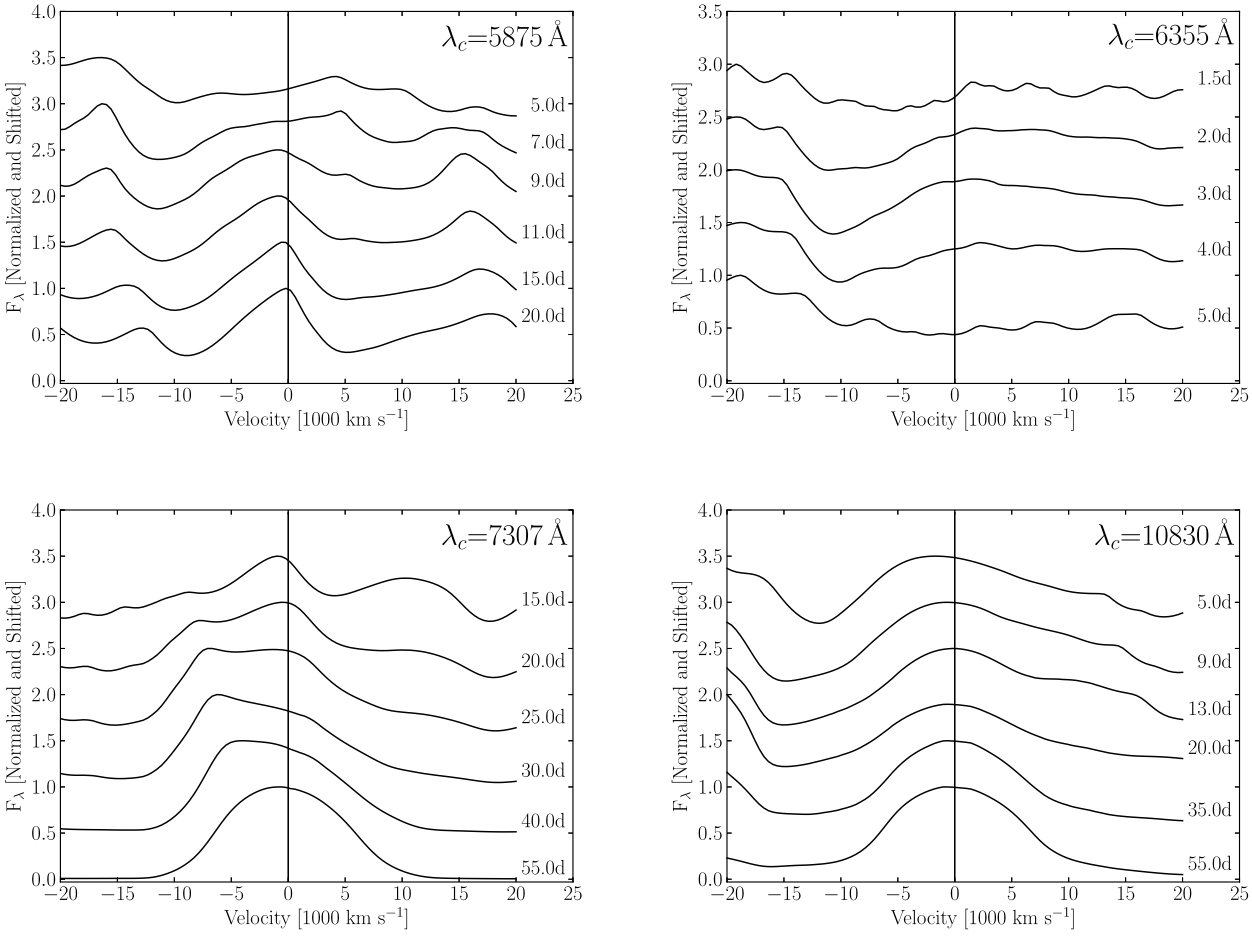

Figure 8. Montage of synthetic spectra for model COp45HEp2, in velocity space, and focusing on specific spectral regions. He I 5875 Å is present over the epochs 5-15 d, and becomes more and more affected by Ti II line absorption (top left). Si II 6355 Å is only visible for a few days after explosion (top right). Ca II 7307 Å develops into a strong line beyond about 20 d after explosion (bottom left). He I 10830 Å is strong at all times beyond 5 d (bottom right).

tical, they can be masked by Ti II line blanketing, which is strong in our model. The notable exception is the enduring He I 10830 Å line. Omitting this aspect, the simulations of Waldman et al. (2011) show comparable optical signatures during the photospheric phase.

8 CALCIUM MASS FROM NEBULAR SPECTRA

In the model spectrum at 55 d, we measure a total luminosity in Ca II 7307 Å of 3.57×10^{39} erg s^{-1}. The expression for the total luminosity in the line is

$$L(\mathrm{Ca\,II}) = h\nu_{ul} N_u A_{ul} \quad (1)$$

where ν_{ul} is the line frequency, N_u is the upper level population and A_{ul} is the radiative de-excitation rate. The critical densities for the Ca II 7291.5–7323.9 Å lines are $4.6–4.0\times10^6$ cm^{-3} at the temperature of 2550 K where the lines form in our ejecta model at 55 d. In the corresponding regions, the electron density is about $1\text{-}1.5\times10^7$ cm^{-3}, thus higher than the critical density. Hence, one can assume that the upper level of each transition is in LTE with respect to the ground state. The above expression then becomes:

$$L(\mathrm{Ca\,II}) = \frac{h\nu_{ul} g_u A_{ul}}{g_l A_{\mathrm{Ca}} m_{\mathrm{u}}} \exp(-h\nu_{ul}/kT) M(\mathrm{Ca}) \quad (2)$$

where g_u and g_l are the statistical weights of the lower and upper transitions, T is the gas temperature, M(Ca) is the total mass of calcium contributing to the line emission, A_{Ca} is the atomic mass of Ca (which we take as 40; the ^{44}Ti has not yet decayed to affect the Ca abundance), and m_{u} is the atomic mass unit. Adopting the value of 0.024 M$_\odot$ for the total calcium mass within 10000 km s^{-1} (see Figs. 1 and 8), we find a theoretical flux of 4.26×10^{39} erg s^{-1}, in good agreement with the line luminosity measured in the theoretical spectrum. Impressively, this Ca II 7307 Å line alone radiates 80 % of the total SN luminosity at that time. The rest of the luminosity in our model comes out in the near-IR, primarily through forbidden transitions of Ti II.

Because Ca II dominates the cooling, and because we do not have a reliable independent means of determining the ejecta temperature (which appears in the exponential) from the observations, it is extremely difficult to determine an accurate calcium mass. In the present model the Ca II line strength is set by the initial mass of ^{48}Cr (which sets the amount of γ-ray energy that can be absorbed) and the ejecta mass and structure (which determines the amount of energy absorbed) in the Ca emitting region. Unfortunately, Ca, Ti, and He all contribute to the γ-ray absorption in the inner region of the ejecta.

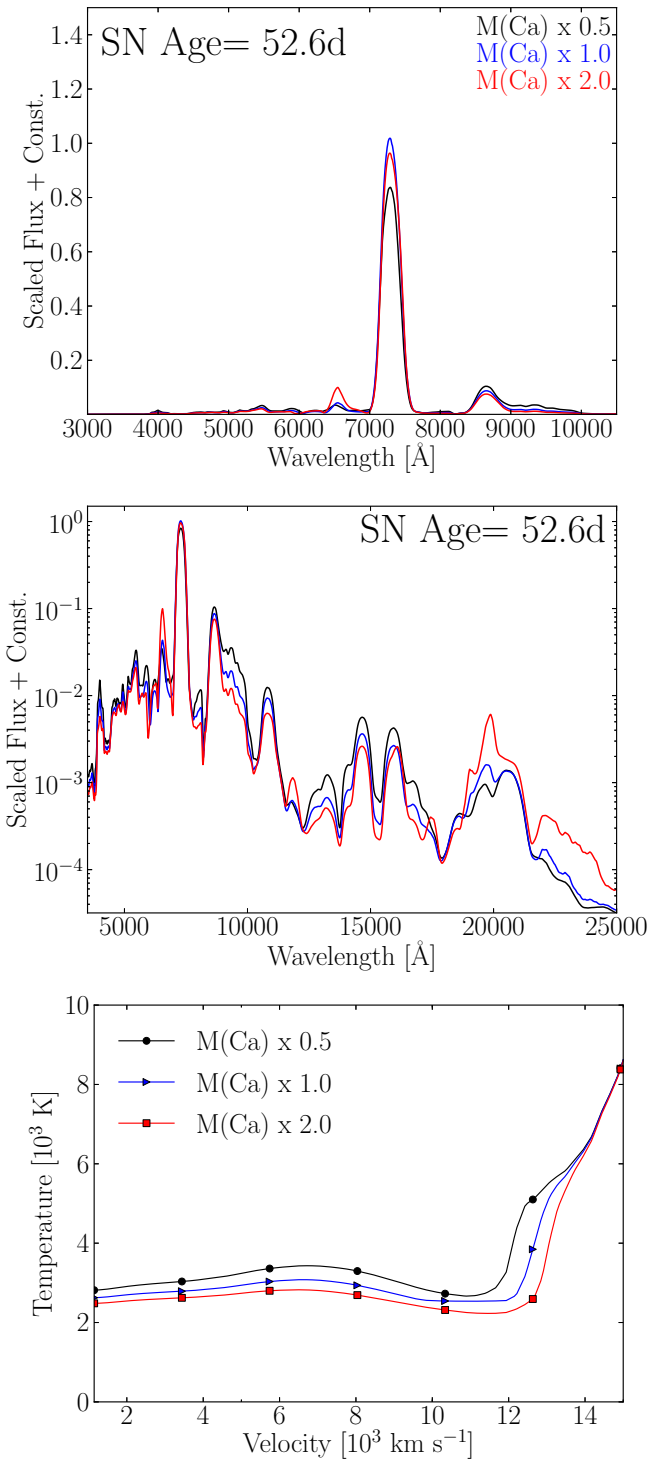

Figure 9. *Top:* Synthetic optical spectra for the model COp45HEp2 at 52.6 d but with a scaling of the Ca abundance by 0.5, 1.0, and 2.0. *Middle:* Same as left, but now for the optical and near-IR ranges, shown on a log scale. *Bottom:* Corresponding temperature profiles. The same color coding applies to all three panels.

We have tested the sensitivity of the emergent spectrum to the calcium abundance. In two additional simulations based on model COp45HEp2 at 52.6 d, we have multiplied the Ca mass fraction throughout the ejecta by a factor of 0.5 and 2.0. In practice, we scale the ^{40}Ca mass fraction and adjust the helium mass fraction (which is large at all depths) to preserve the normalization to unity (in practice, this also impacts the γ-ray trapping but we neglect this effect for this simple test). We find that the flux in the Ca II 7307 Å line varies by only ~ 10 % between these simulations (Fig. 9) and that this line remains the main coolant in each case — a reduction in flux of the Ca II 7307 Å line is compensated by an increase in the near-IR flux of forbidden lines of Ti II (for a large enhancement in Ca mass fraction, the Ca ionization can shift and allow for cooling through Ca I lines as well). Rather than changing the Ca II line flux, varying the total Ca mass causes a change in temperature. This weak sensitivity of the Ca II 7307 Å line flux to the calcium abundance results from the fact that this line is the main coolant. As long as this holds, the corresponding Ca II line flux reflects primarily the trapped decay energy (which must be radiated) and only more weakly the Ca abundance.

9 OXYGEN MASS FROM NEBULAR SPECTRA

Our model has a very low oxygen mass, and consequently we do not predict any emission in [O I] 6300–6364 Å. This doublet line seems to be present at nebular times in both PTF10iuv and SN 2005E.

In order to get O emission two criteria need to be met. First, we need a significant amount of O in a region where γ-rays are being absorbed. Second, the O emitting region cannot be too contaminated by Ca. The [Ca II] doublet at 7307 Å is a much more efficient coolant than [O I] 6300 Å (by nearly a factor of 1000 per atom in the high density limit), and thus can limit the strength of [O I] 6300–6364 Å emission from a region in which both Ca^{+} and O^{0+} co-exist (Fransson & Chevalier 1989). While oxygen features are readily identified in photospheric phase spectra of SN 2008ha, [O I] 6300 Å is absent from the spectrum at 62 days (Foley et al. 2009) in SN 2008ha (but present in SN 2005E).

An estimate of the oxygen mass, in the high density limit, can be made using

$$M[\mathrm{O}] = 1.1 \times 10^{8} \mathrm{f}_{[\mathrm{O\,I}]} \mathrm{D}^{2}_{\mathrm{Mpc}} \exp(2.78/\mathrm{T}_{4}) \qquad (3)$$

where $f_{[\mathrm{O\,I}]}$ is the total flux in the [O I] 6300–6364 doublet, D_{Mpc} is the distance to the SN in Mpc, and T_4 is the temperature in 10^4 K — this expression is very similar to the one given by Uomoto (1986). In practice this is, however, not a particularly useful expression since the derived O mass is very sensitive to temperature (just like for the Ca mass estimate; see preceding section). For SN 2005E, Perets et al. (2010) estimate an oxygen mass of 0.037 $M_\odot$ and use $T_4 = 0.45$. If we were to adopt the temperature of 2550 K in the [Ca II] emitting zone of our model, this mass estimate would be 110 times larger, which is unrealistic.

In reality, the emission regions of [O I] and [Ca II] are probably distinct. The O I emission strength will be primarily set by the non-thermal energy absorbed in the corresponding region. A fundamental requirement of any model to explain SN 2005E is that the ejecta have a significant amount of O, and this O lies outside the [Ca II] emitting region. The uncertainty that surrounds the origin of these fast transients, in particular concerning the explosion mechanism and the importance of multi-D effects, prevent a clear

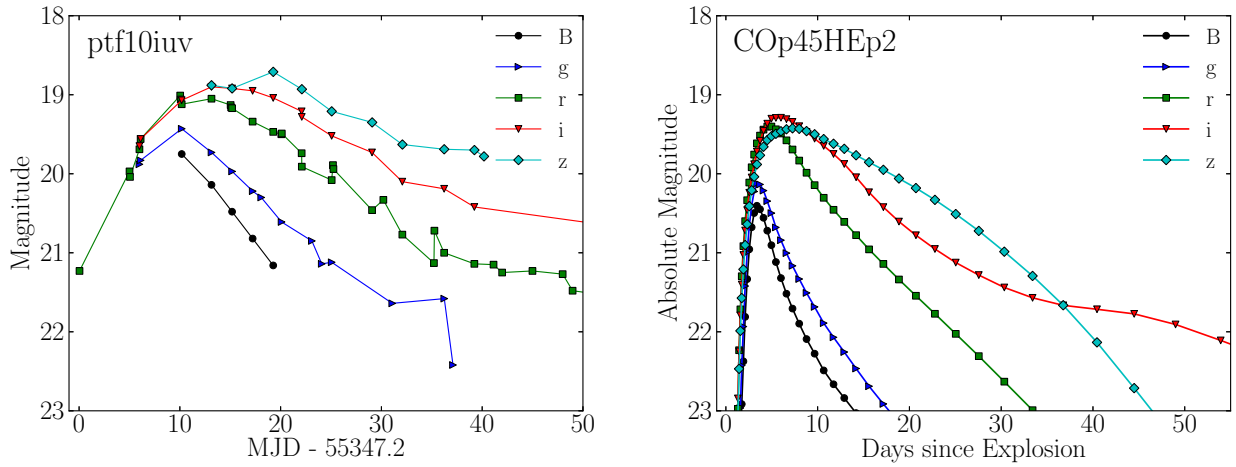

Figure 10. *Left:* Multi-band light curves of PTF10iuv (Kasliwal et al. 2012). *Right:* Synthetic photometry for model COp45HE2 but scaled to match the distance and redshift to PTF10iuv. While model COp45HEp2 exhibits a rapid rise like PTF10iuv it is too faint, and fades more rapidly. This discrepancy suggests the model ejecta mass is too small. [See text for details.]

determination of the spatial distribution of O and Ca, which in turn compromises the accuracy of the O abundance determination.

10 COMPARISON TO OBSERVATIONS AND CONCLUSIONS

Numerical simulations of He-shell detonations suggest a wide range of ejecta yields and masses (Fink et al. 2007; Shen et al. 2010; Waldman et al. 2011). The outcome is function of both the WD mass and the He-shell mass, and thus theoretical models can yield a large diversity of transient light curves and spectra.

Observationally, Ca-rich transients show a common set of properties (Kasliwal et al. 2012), in particular the faint peak luminosity, a fast rise to maximum, a narrow light curve width, fast expansion, and a preponderance of Ca II lines in nebular-phase optical spectra. All of these properties are a suitable description of .Ia SN models.

The multi-band light curves of PTF10iuv show a moderate resemblance to those of model COp45HE2 (Fig. 10). For example, both observations and model exhibit a time to maximum brightness that increases for redder filters. The model peak brightness is within 0.5-1 mag of the observed value, depending on the filter. Important disagreements are the longer rise to peak, the broader and the more slowly declining light curves (in all bands) observed in PTF10iuv compared to the model. These mismatches are also present if we compare to SN 2005E (Perets et al. 2010).

In Fig. 11, we compare model spectra with observations (at comparable epochs with respect to maximum brightness) for PTF10iuv, SN 2005E, and PTF09dav. Observed pre-peak spectra tend to be bluer than in the model. Our model is red even at peak, which is expected given the high metal abundance from the explosion.[2] However, this makes it hard to compare to early-time observations because the temperature difference is tied to an ionization offset and thus different ions/lines influence the spectra. He I lines, which stem from non-thermal processes, are predicted by the model, but the observations show their presence for much longer. The model predicts strong blanketing due to Ti II, stronger than observed, which suggests Ca-rich transients in Nature may have a lower mass fraction of metals than in our model. In PTF09dav, Sc II lines are clearly visible (Sullivan et al. 2011) but are weak or absent in our model. The spectral differences at early time between PTF10iuv and PTF09dav suggests that there is diversity in Nature amongst Ca-rich transients, likely stemming from variations in burning yields.[3]

Models and observations agree well at nebular times in that they both show a dominance of Ca II lines. We note a few discrepancies between synthetic and observed spectra at nebular times. The Ca II line at 7307 Å is broader in the model than observed. The half-width at zero flux is ~ 5000 km s^{-1} in PTF10iuv compared to ~ 10000 km s^{-1} in the model. The Ca II forbidden-line doublet (Ca II triplet at 8500 Å) also appears (disappears) much earlier than in the observations. Furthermore, our model has a very low O mass, and consequently does not predict the [O I] 6300–6364 Å that seems to be present at nebular times in PTF10iuv and SN 2005E.

Together with the mismatches in early-time color, light curve width, and post-peak decline rate, these spectral differences suggest that the ejecta mass of these Ca-rich transients is most likely larger than 0.2 $M_\odot$ and the helium shell more extended initially. The fainter peak of our model could be cured by a larger ^{48}Cr. Waldman et al. (2011) argue that by enhancing the Ti abundance, the post-peak brightness could be brought into agreement with the observations of SN 2005E. However, this solution is unlikely because the Ti II lines are already stronger in the model than in the observations. A lower expansion rate and thus a lower explosion energy would also help reconcile some of the mismatches, but our model is already too faint compared to PTF10iuv. So, it seems a

[2] To test the influence of Ti, we artificially scaled down its abundance in the formal solution of the radiative transfer, i.e., to calculate the emergent spectrum. Scaling it down by a factor of 0.1 or 0.01 in the model at 5.9 d makes the spectrum increasingly bluer (in this order, the $V-I$ magnitude varies from 0.74 mag to 0.55 and 0.30 mag) , and the Ti II lines in the red weaker.

[3] Our model results are in closer agreement with the observations of OGLE-2013-SN-079, which show red colors and a spectrum apparently influenced by strong Ti II line blanketing (Inserra et al. 2014). We do not discuss this object in detail here because the paper by Inserra et al. was submitted while this work was under review.

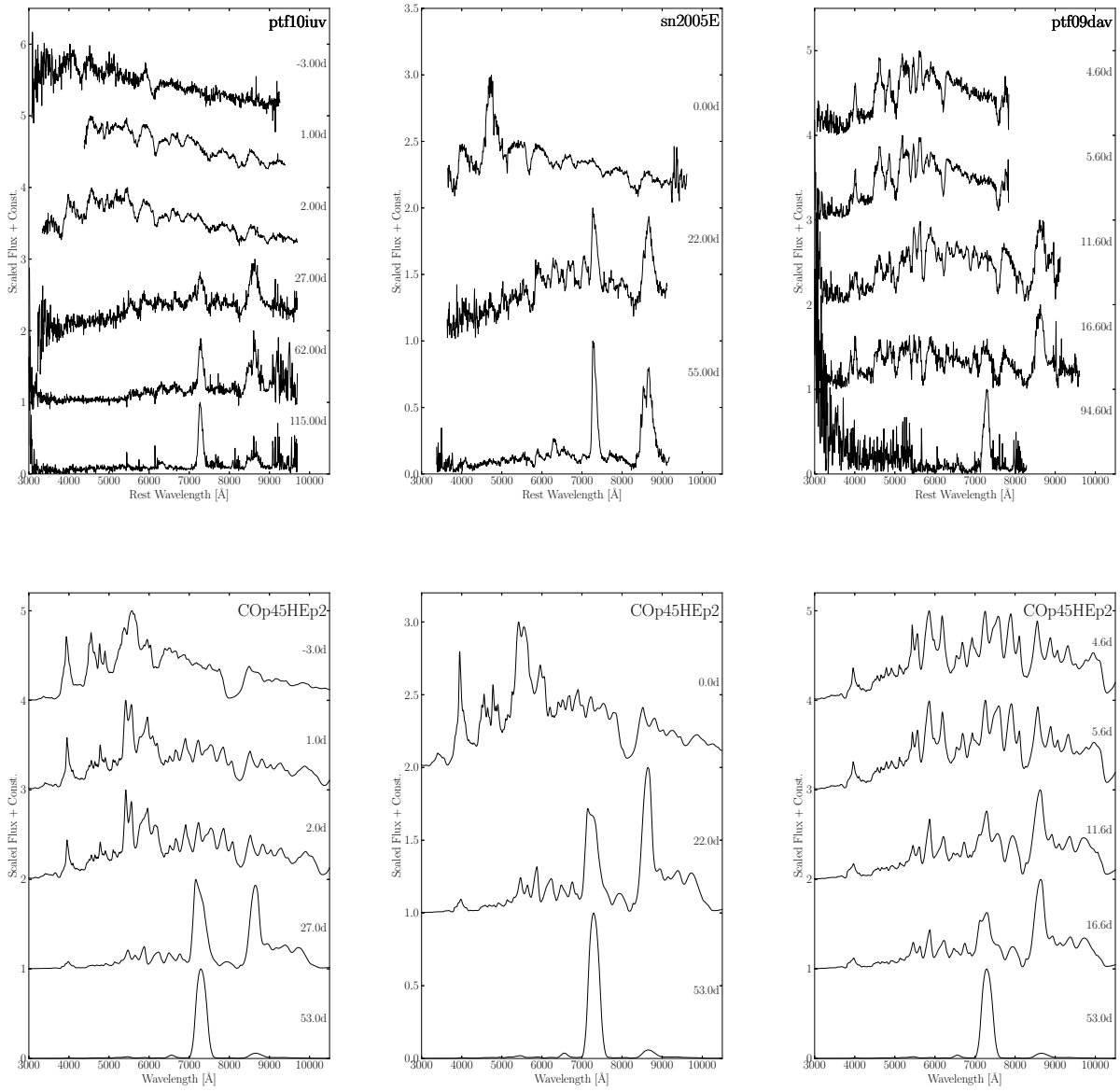

Figure 11. *Top row:* Montage of rest-frame spectra for PTF10iuv (Kasliwal et al. 2012), SN 2005E (Perets et al. 2010), and PTF09dav (Sullivan et al. 2011). *Bottom row:* Montage of spectra for model COp45HEp2 shown at epochs that correspond to those of observations, column by column. The plots are offset vertically, and for each plot the associated zero is set at 3000 Å. [See text for details.]

higher ejecta mass is really needed to get the broader light curve, yielding a slower expansion rate that also agrees better with the relatively narrow line profiles observed.

Most estimates for the ejecta mass of Ca-rich transients typically assume that the opacity is the same as in standard SNe Ia. However, the opacity of standard SNe Ia is dominated by IGEs, and to a lesser extent, IMEs. Conversely, our He shell detonation model has a large He abundance, and hence we would expect a significantly lower opacity (Fig. 12; see also bottom left panel of Fig. 2). The ejecta mass inferred from the light curve scales as $1/\kappa$ (the light curve morphology is sensitive to optical depth, which goes as $M\kappa$; Arnett 1982), so ejecta masses based on scaling from normal SNe Ia will tend to underestimate the true ejecta mass.

A crucial question, which should be obtainable from accurate light curves and spectral modeling, is what are the radioactive isotopes that heat the SN ejecta and produce the bright display. One needs to determine the relative contributions from, for example, the decay chain associated with ^{56}Ni (which powers standard SNe Ia light curves), and the decay chain associated with ^{48}Cr.

One interesting possibility is that these Ca-rich transients do not stem from a detonation of an helium-accreting CO WD, but instead from the merger of a CO WD and a He WD (see the merger simulations, e.g., of Pakmor et al. 2013). The lighter He WD is less dense and gets completely disrupted during the coalescence. When He eventually comes to rest at the surface of the CO remnant, a detonation is somehow born (just like in the He-shell model) giving rise to an explosion in an extended and much more massive He shell. The detonation inside an extended shell would

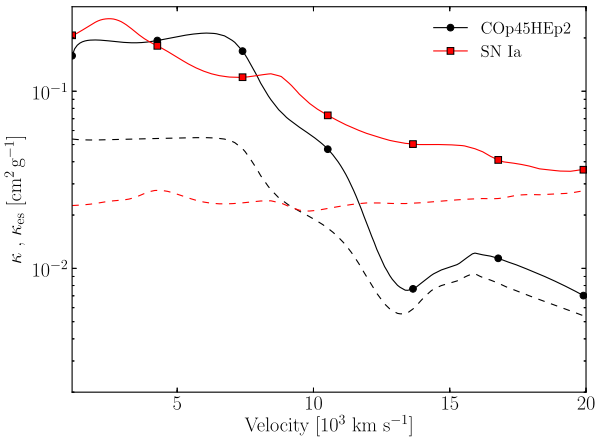

Figure 12. Comparison of the total opacity (i.e., mass absorption coefficient κ) and the electron scattering opacity (κ_{es}; dashed line) between the He-detonation model COp45HEp2 and the standard-luminosity SN Ia model DDC10 (Dessart et al. 2014c) at the time of bolometric maximum. The difference at large velocities stems from the low ionization in the COp45HEp2 model. The similarity at lower velocities is a combination of several effects. Line opacity from IGEs in a SN Ia ejecta is large but this is offset by the larger mean atomic weight. These regions are also ionized and optically thick at maximum light in both models so electron scattering matters, and its contribution is larger in the He-detonation model.

likely cause some exchange from kinetic energy into internal energy, as in pulsational-delayed-detonation models of SNe Ia or in WD explosions within a buffer of mass (see, e.g., Fryer et al. 2010), and contribute excess luminosity and bluer colors at early times (Hoeflich & Khokhlov 1996; Dessart et al. 2014a). The greater mass of the He shell would cause a more efficient trapping of γ-rays and thus a more sustained brightness past peak, in better agreement with observations of Ca-rich transients.

ACKNOWLEDGMENTS

We acknowledge discussions with Carles Badenes, Ryan Foley, Mansi Kasliwal, and Roni Waldman. We thank Roni Waldman and Eli Livne for providing model COp45HEp2, and the observers for making their data public through WISEREP. LD acknowledges financial support from the European Community through an International Re-integration Grant, under grant number PIRG04-GA-2008-239184, and from "Agence Nationale de la Recherche" grant ANR-2011-Blanc-SIMI-5-6-007-01. DJH acknowledges support from STScI theory grant HST-AR-12640.01, and NASA theory grant NNX14AB41G. This work was supported in part by the National Science Foundation under Grant No. PHYS-1066293 and the hospitality of the Aspen Center for Physics. This work was granted access to the HPC resources of CINES under the allocations c2013046608 and c2014046608 made by GENCI (Grand Equipement National de Calcul Intensif).

REFERENCES

Anderson, J. P. & James, P. A. 2009, MNRAS, 399, 559
Arnett, W. D. 1982, ApJ, 253, 785
Bildsten, L., Shen, K. J., Weinberg, N. N., & Nelemans, G. 2007, ApJL, 662, L95
Blondin, S., Dessart, L., Hillier, D. J., & Khokhlov, A. M. 2013, MNRAS, 429, 2127
Dessart, L., Blondin, S., Hillier, D. J., & Khokhlov, A. 2014a, MNRAS, 441, 532
Dessart, L. & Hillier, D. J. 2005, A&A, 437, 667
—. 2008, MNRAS, 383, 57
—. 2010, MNRAS, 405, 2141
—. 2011, MNRAS, 410, 1739
Dessart, L., Hillier, D. J., Blondin, S., & Khokhlov, A. 2014b, MNRAS, 441, 3249
—. 2014c, MNRAS, 441, 3249
Dessart, L., Hillier, D. J., Li, C., & Woosley, S. 2012, MNRAS, 424, 2139
Fink, M., Hillebrandt, W., & Röpke, F. K. 2007, A&A, 476, 1133
Fink, M., Kromer, M., Seitenzahl, I. R., Ciaraldi-Schoolmann, F., Röpke, F. K., Sim, S. A., Pakmor, R., Ruiter, A. J., & Hillebrandt, W. 2014, MNRAS, 438, 1762
Foley, R. J., Challis, P. J., Chornock, R., Ganeshalingam, M., Li, W., Marion, G. H., Morrell, N. I., Pignata, G., Stritzinger, M. D., Silverman, J. M., Wang, X., Anderson, J. P., Filippenko, A. V., Freedman, W. L., Hamuy, M., Jha, S. W., Kirshner, R. P., McCully, C., Persson, S. E., Phillips, M. M., Reichart, D. E., & Soderberg, A. M. 2013, ApJ, 767, 57
Foley, R. J., Chornock, R., Filippenko, A. V., Ganeshalingam, M., Kirshner, R. P., Li, W., Cenko, S. B., Challis, P. J., Friedman, A. S., Modjaz, M., Silverman, J. M., & Wood-Vasey, W. M. 2009, AJ, 138, 376
Fransson, C. & Chevalier, R. A. 1989, ApJ, 343, 323
Fryer, C. L., Ruiter, A. J., Belczynski, K., Brown, P. J., Bufano, F., Diehl, S., Fontes, C. J., Frey, L. H., Holland, S. T., Hungerford, A. L., Immler, S., Mazzali, P., Meakin, C., Milne, P. A., Raskin, C., & Timmes, F. X. 2010, ApJ, 725, 296
Hillier, D. J. & Dessart, L. 2012, MNRAS, 424, 252
Hoeflich, P. & Khokhlov, A. 1996, ApJ, 457, 500
Inserra, C., Sim, S. A., Wyrzykowski, L., Smartt, S. J., Fraser, M., Nicholl, M., Shen, K. J., Jerkstrand, A., Gal-Yam, A., Howell, D. A., Maguire, K., Mazzali, P., Valenti, S., Taubenberger, S., Benitez-Herrera, S., Bersier, D., Blagorodnova, N., Campbell, H., Chen, T.-W., Elias-Rosa, N., Hillebrandt, W., Kostrzewa-Rutkowska, Z., Kozlowski, S., Kromer, M., Lyman, J. D., Polshaw, J., Ropke, F. K., Ruiter, A. J., Smith, K., Spiro, S., Sullivan, M., Yaron, O., Young, D., & Yuan, F. 2014, arXiv:1410.6473
Jordan, IV, G. C., Perets, H. B., Fisher, R. T., & van Rossum, D. R. 2012, ApJL, 761, L23
Kasliwal, M. M., Kulkarni, S. R., Gal-Yam, A., Nugent, P. E., Sullivan, M., Bildsten, L., Yaron, O., Perets, H. B., Arcavi, I., Ben-Ami, S., Bhalerao, V. B., Bloom, J. S., Cenko, S. B., Filippenko, A. V., Frail, D. A., Ganeshalingam, M., Horesh, A., Howell, D. A., Law, N. M., Leonard, D. C., Li, W., Ofek, E. O., Polishook, D., Poznanski, D., Quimby, R. M., Silverman, J. M., Sternberg, A., & Xu, D. 2012, ApJ, 755, 161
Li, C., Hillier, D. J., & Dessart, L. 2012, MNRAS, 426, 1671
Livne, E. & Arnett, D. 1995, ApJ, 452, 62
Livne, E. & Glasner, A. S. 1990, ApJ, 361, 244
—. 1991, ApJ, 370, 272
Lucy, L. B. 1991, ApJ, 383, 308
Milne, P. A., The, L.-S., & Leising, M. D. 1999, ApJS, 124, 503
Mulchaey, J. S., Kasliwal, M. M., & Kollmeier, J. A. 2014, ApJL, 780, L34

Pakmor, R., Kromer, M., Taubenberger, S., & Springel, V. 2013, ApJL, 770, L8
Perets, H. B. 2014, arXiv:1407.2254
Perets, H. B., Gal-yam, A., Crockett, R. M., Anderson, J. P., James, P. A., Sullivan, M., Neill, J. D., & Leonard, D. C. 2011, ApJL, 728, L36
Perets, H. B., Gal-Yam, A., Mazzali, P. A., Arnett, D., Kagan, D., Filippenko, A. V., Li, W., Arcavi, I., Cenko, S. B., Fox, D. B., Leonard, D. C., Moon, D.-S., Sand, D. J., Soderberg, A. M., Anderson, J. P., James, P. A., Foley, R. J., Ganeshalingam, M., Ofek, E. O., Bildsten, L., Nelemans, G., Shen, K. J., Weinberg, N. N., Metzger, B. D., Piro, A. L., Quataert, E., Kiewe, M., & Poznanski, D. 2010, Nature, 465, 322
Shen, K. J., Kasen, D., Weinberg, N. N., Bildsten, L., & Scannapieco, E. 2010, ApJ, 715, 767
Sim, S. A., Fink, M., Kromer, M., Röpke, F. K., Ruiter, A. J., & Hillebrandt, W. 2012, MNRAS, 420, 3003
Sullivan, M., Kasliwal, M. M., Nugent, P. E., Howell, D. A., Thomas, R. C., Ofek, E. O., Arcavi, I., Blake, S., Cooke, J., Gal-Yam, A., Hook, I. M., Mazzali, P., Podsiadlowski, P., Quimby, R., Bildsten, L., Bloom, J. S., Cenko, S. B., Kulkarni, S. R., Law, N., & Poznanski, D. 2011, ApJ, 732, 118
Taam, R. E. 1980, ApJ, 237, 142
Uomoto, A. 1986, ApJL, 310, L35
Waldman, R., Sauer, D., Livne, E., Perets, H., Glasner, A., Mazzali, P., Truran, J. W., & Gal-Yam, A. 2011, ApJ, 738, 21
Woosley, S. E. & Weaver, T. A. 1994, ApJ, 423, 371
Xu, Y., Ross, R. R., & McCray, R. 1991, ApJ, 371, 280
Yaron, O. & Gal-Yam, A. 2012, PASP, 124, 668